

# Leaky Least Logarithmic Absolute Difference Based Control Algorithm and Learning Based InC MPPT Technique for Grid Integrated PV System

Nishant Kumar, *Member IEEE*, Bhim Singh, *Fellow IEEE*, Bijaya Ketan Panigrahi, *Senior Member IEEE*, and L. Xu, *Senior Member, IEEE*

**Abstract**—This work introduces a novel Leaky Least Logarithmic Absolute Difference (LLAD) based control algorithm and Learning based Incremental Conductance (LIC) MPPT (Maximum Power Point Tracking) algorithm, for grid-integrated solar PV (Photovoltaic) system. Here, a three-phase topology of grid-integrated PV system is implemented, with the nonlinear/linear loads. Proposed LIC technique is an improved form of an Incremental Conductance (InC) algorithm, where inherent problems of traditional InC technique like steady-state oscillations, slow dynamic responses and fixed step size issues, are successfully mitigated. The prime objective of proposed LLAD control is to meet the active power requirement of the loads from generated solar PV power, and after satisfying the load demand, the excess power is supplied to the grid. However, when generated solar power is less than the load demand, then LLAD meets the load by taking extra required power from the grid. During these power management processes, on the grid side, the power quality is maintained. During daytime, the proposed control technique provides load balancing, power factor correction, and harmonics filtering. Moreover, when solar irradiation is zero, then the DC link capacitor and VSC, act as DSTATCOM (Distribution Static Compensator), which enhances the utilization factor of the system. The proposed techniques are modeled, and their performances are verified experimentally on a developed prototype, in solar insolation variation conditions, unbalanced loading, as well as in different grid disturbances such as over and under-voltage, phase imbalance, harmonics distortion in the grid voltage etc. Test results have met the objectives of proposed work and parameters are under the permissible limit, according to the IEEE-519 standard.

**Index Terms**—Solar PV Array, Power Quality, Grid Integrated System, InC, MPPT.

## I. INTRODUCTION

POWER generation and distribution systems are undergoing substantial changes, because of modern technology and new advents, such as integration of large-scale renewable distributed generations, advanced communication and control schemes, and large storage capability. Out of several renewable resources, due to the static structure, small size and almost zero maintenance cost, solar PV (Photovoltaic) based energy generating system is highly popular [1]. The available literature reveals that out of several ways of grid integration of solar PV system, a two-stage topology is the most popular way of synchronization, where two converters are used. One DC-DC converter is used for maximum power point tracking (MPPT), and another DC-AC converter is used for power conversion as well as grid synchronization. Two-stage topology is popular, because, here DC link voltage and PV voltage are different, so a two-stage system can work with any rating of the PV array. In case of high PV voltage fluctuation condition, a two-stage

system is the only option for operating in constant DC link voltage condition. Moreover, due to two separate controls for the DC-DC converter (such as a boost converter) and the DC-AC converter such as for VSC (Voltage Source Converter), the overall control complexity is very less [2][3].

However, for optimal operation of DC-AC converter (VSC), an efficient control technique is needed. The prime objective of the control technique is that the generated solar power is supplied to the nearby loads and, after satisfying the load demand the rest power is supplied to the grid. However, when generated solar power is not sufficient for the load, then the load requirement is met by taking extra required power from the grid. In this process, the responsibilities of the control technique, are, (1) power conversion from DC to AC, (2) to follow the grid code for synchronization with the grid, (3) power quality improvement of the supply power, (4) to act as DSTATCOM (Distribution Static Compensator), when solar irradiation low, and (5) power management. It provides power factor correction, harmonics filtering and mitigation of other power quality issues.

In-depth literature review on ‘control techniques for the grid integrated solar PV system’ depicts that recently, researchers have proposed several adaptive control algorithms [4], such as fuzzy adaptive control [5], learning based control [6], power delta control etc. However, for abnormal grid conditions, the performances of these control techniques, are not reported, which is the essential phenomenon of the distribution grid. The other control techniques like, discrete-Fourier transform (DFT), PM (Prony’s method), frequency locked loop (FLL) [7], second-order generalized integrator (SOGI) [8] and Kalman filter (KF) [9] have been proposed to handle the abnormal grid condition. However, none of these techniques, is suitable for all types of grid adverse conditions, such as FLL and SOGI based control techniques are unable to handle lower order harmonics and DC offset [10]. The fixed length window with stationary waveform is required for searching in DFT based control technique, which is not suitable for online searching. The performance of PM is appreciable in different grid adverse conditions. However, in the PM technique, the higher order polynomial equation and its solution process, create a huge computational burden on the processor, which is not suitable for the low-cost microcontroller. Similarly, KF based control technique is good for solution estimation using correction and prediction process. Moreover, the modified version of KF, like extended KF [11] and linear KF [12] based control techniques are also good for the integrated grid system. However, during state variable estimation, linearization, prediction and correction, the derivative properties are used, which is the

source of burden and the algorithm complexity on the processor. Therefore, a heavy computational burden arises on the processor, which is not suitable for a low-cost microcontroller. Model predictive control technique [13] is also popular for good steady-state response, but during dynamic condition, its responses are poor, due to its predictive nature, which is based on the previous dataset. Similarly, resonant controllers, for tracking the sinusoidal inverter current, in grid connected system has been presented in [14], which shows a good steady state response with low harmonics content in injected grid current. However, during transient condition, the performance rapidly deteriorates, due to the changes in the grid frequency.

Therefore, in this paper, a novel Leaky Least Logarithmic Absolute Difference (LLLAD) based control algorithm is proposed for efficient and robust operation of grid-integrated solar PV system. This technique is free from the derivative term, so the computational burden is low, as well as the performance of LLLAD control is instantaneous and suitable for the high-frequency system.

Moreover, in this paper, a Learning-based Incremental Conductance (LIC) based Maximum Power Point Tracking (MPPT) algorithm is proposed. This LIC is the improved form of Incremental Conductance (InC) algorithm, which mitigates the inherent problems of traditional InC algorithm [15], like steady-state oscillation, slow dynamic responses and fixed step size issues. A literature review on MPPT shows that many authors have tried to solve these problems through some modifications in classical algorithms namely, modified perturb and observed (P&O) [16], improved InC [17], fuzzy logic based MPPT[18], artificial intelligence based MPPT approach [19], *etc.* However, still, an optimum solution has not come. Because, if few improved techniques are performing well in the steady state then these are lagging during dynamics, vice versa. Moreover, few techniques are performing relatively well, but the huge computational complexity and large design constraints, restrict to perform on the low-cost processor. Therefore, LIC algorithm is proposed, which simple structure is easy in implementation and its learning nature decides the size of step change according to the situation, such as step size decreases during steady state condition, and step size increases during dynamic changes.

In this work, the merits of LLLAD control algorithm and LIC MPPT technique are verified experimentally on a developed prototype in solar irradiation variation conditions, imbalanced condition of linear/nonlinear loads, as well as in different grid disturbances such as voltage unbalances, phase imbalances, harmonics distortion in grid voltage etc. Test results and analysis show a very good and optimal power management. However, the drawback is, high algorithm complexity of the proposed control technique w.r.t. state of the art techniques. Therefore, for easy implementation and to reduce the algorithm complexity, the block diagram of LLLAD for the active component extraction has been given and described in section II(B).

## II. SYSTEM LAYOUT

A two-stage topology of three-phase grid-tied solar PV system is given in Fig.1, where solar PV power is supplied to the grid, through a DC-DC converter and a three-phase voltage source converter (VSC) in such a way that the operating point of PV

array is at MPP (Maximum Power Point) and, the converter power is synchronized to the grid. Here for control, LIC MPPT algorithm is used for the DC-DC converter, and LLLAD based control algorithm is used for the DC-AC VSC. In this configuration, at the point of common coupling (PCC), ripple filter ( $C_r$ ,  $R_r$ ), grid through interfacing inductor ( $L_{VSC}$ ,  $R_{VSC}$ ), load and output terminal of VSC are connected. Here, the ripple filter is used for absorbing switching ripples, which are produced by VSC. The main objectives of control scheme, are during PV power generation, the power is fed to the grid in UPF (Unity Power Factor) mode of operation, and when PV power is unavailable then it operates in DSTATCOM (Distribution Static Compensator) mode.

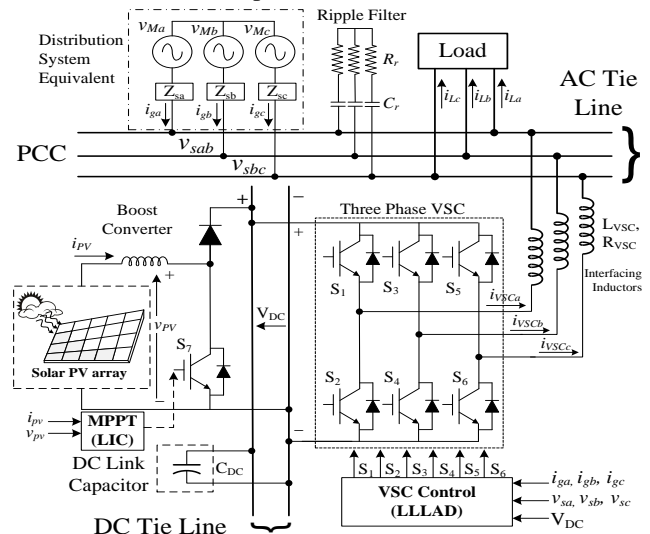


Fig.1 Three-Phase Grid-tied Solar Energy Conversion System.

## III. CONTROL APPROACH

In the proposed control scheme, two separate control strategies are used for the boost converter and for VSC, which is shown in Fig.2. For boost converter, a novel LIC MPPT technique is used for maximum power harvesting from the solar PV array. Moreover, for VSC, a novel LLLAD based control strategy is used for UPF operation. Here, LLLAD algorithm is used for extraction of fundamental component from load current and estimation of grid reference currents.

First, LIC MPPT technique is used for the boost converter, which produces a reference voltage ( $V_{ref}$ ), for operating on maximum power.

For keeping constant DC link voltage ( $V_{DCref}$ ) and to operate at  $V_{ref}$ , an optimal duty cycle ( $\beta$ ) is calculated, which is described as,

$$\beta = 1 - \frac{V_{ref}}{V_{DCref}} \quad (1)$$

For generating switching signal for the boost converter ( $S_7$ ), the sawtooth signal and calculated  $\beta$  are compared, which generates switching pulse.  $V_{DCref}$  is calculated [20] as,

$$V_{DCref} = \sqrt{3} \times \theta \times V_x \quad (2)$$

Where,  $V_x$  is amplitude of the grid voltage, and  $\theta$  is loss compensation component.

After this, by using a bandpass filter, the fundamental components of PCC voltages ( $v_a$ ,  $v_b$ ,  $v_c$ ) are extracted from the grid line voltages ( $v_{sa}$ ,  $v_{sb}$ ,  $v_{sc}$ ). These  $v_a$ ,  $v_b$ , and  $v_c$  are in-phase quantities of  $v_{sa}$ ,  $v_{sb}$ , and  $v_{sc}$ . The transfer function of the bandpass filter is derived as,

$$T_f = \frac{k(z-1)}{z^2 + (k-2)z + \left(1-k + \frac{k^2}{2}\right)} \quad (3)$$

Where,  $k = \sqrt{2} \times \omega \times T_s$ ,  $T_s$  and  $\omega$  are sampling period and natural frequency ( $2\pi f$ ), respectively.

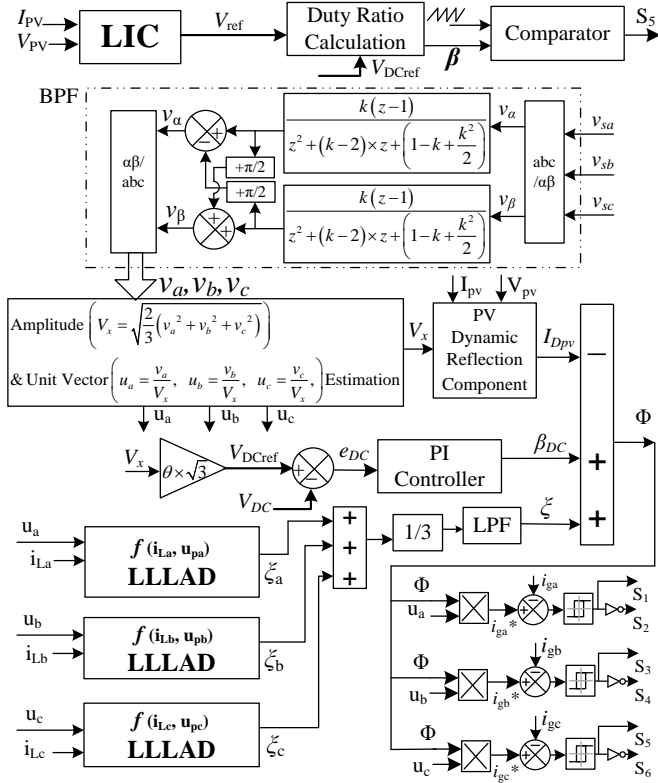


Fig.2 Control scheme for grid-integrated solar power generation system.

For improving the dynamic performances, by using the solar PV dynamic reflection component ( $I_{Dpv}$ ), the impact of the instantaneous reflection in PV power ( $P_{pv}$ ) on the grid current is taken under consideration, which is derived as,

$$I_{Dpv} = \frac{2 \times V_{pv} \times I_{pv}}{3 \times V_x} \quad (4)$$

For maintaining the DC link voltage,  $V_{DCref}$  is compared with the sensed DC link voltage ( $V_{DC}$ ), which generates DC link voltage error ( $e_{DC} = V_{DCref} - V_{DC}$ ). This  $e_{DC}$  is fed to the PI (Proportional Integral) controller, which gives the value of the DC loss component ( $\beta_{DC}$ ), as,

$$\beta_{DC}(n+1) = G_p \times e_{DC}(n) + G_i \sum_{n=0}^i e_{DC}(n) \quad (5)$$

Where,  $G_p$  and  $G_i$  are proportional and integral gains of the PI controller, which regulates DC link voltage.

For estimating active weight components ( $\xi_a$ ,  $\xi_b$ ,  $\xi_c$ ), three separate LLLAD control blocks are used, which are the function of load currents ( $i_{La}$ ,  $i_{Lb}$ ,  $i_{Lc}$ ), in-phase unit-templates ( $u_a$ ,  $u_b$ ,  $u_c$ ).

$$\left. \begin{aligned} [\xi_a] &\Rightarrow f_{LLLAD}(i_{La}, u_a) \\ [\xi_b] &\Rightarrow f_{LLLAD}(i_{Lb}, u_b) \\ [\xi_c] &\Rightarrow f_{LLLAD}(i_{Lc}, u_c) \end{aligned} \right\} \quad (6)$$

The resultant estimated active weight component ( $\xi$ ) and resultant active weight component ( $\Phi$ ) are calculated as,

$$\xi = \frac{1}{3}(\xi_a + \xi_b + \xi_c) \quad (7)$$

$$\Phi = \beta_{DC} + \xi - I_{Dpv} \quad (8)$$

The reference grid currents ( $i_{ga}^*$ ,  $i_{gb}^*$ ,  $i_{gc}^*$ ) are generated as,

$$i_{ga}^* = \Phi \times u_a, \quad i_{gb}^* = \Phi \times u_b, \quad i_{gc}^* = \Phi \times u_c \quad (9)$$

The switching pulses ( $S_1$ ,  $S_2$ ,  $S_3$ ,  $S_4$ ,  $S_5$ , and  $S_6$ ) of voltage source converter are generated by using hysteresis controller [21], where the input signals are grid currents ( $i_{ga}$ ,  $i_{gb}$ ,  $i_{gc}$ ) and  $i_{ga}^*$ ,  $i_{gb}^*$ ,  $i_{gc}^*$ .

### A. Learning-Based Incremental Conductance (LIC) Algorithm

The efficiency of the solar PV array is improved by using a MPPT algorithm, which forces it to operate at the maximum power point. The most popular MPPT techniques are P&O, and Inc. However, the problems with these techniques are steady-state oscillations, slow dynamic response and fixed step size issues. Therefore, for mitigating all above problems, a novel LIC algorithm is proposed here.

Fig.3 shows the working strategy of LIC technique, which is divided into two parts. The 1<sup>st</sup> section deals with the steady state condition, where steady-state oscillations are mitigated, by reducing the size of the step change. Moreover, the 2<sup>nd</sup> section deals with the dynamic condition after that it quickly jumps on the required duty cycle, by increasing the size of the step change. For sensing the condition, an envelope is created in each iteration, whose upper and lower bands are  $lu$  and  $ll$ , respectively.  $lu$  and  $ll$  are calculated according to the base step size ( $d_{base}$ ), which is taken as a fixed size of step change in conventional Inc.  $lu$  and  $ll$  are described as,

$$lu = \left( 100 + \left( \left( \frac{V_{oc}}{1 - d_{base}} \right) - V_{oc} \right) \times \frac{100}{V_{mpp}} \right) \times \frac{1}{100} \quad (10)$$

$$ll = \left( 100 - \left( \left( \frac{V_{oc}}{1 - d_{base}} \right) - V_{oc} \right) \times \frac{100}{V_{mpp}} \right) \times \frac{1}{100} \quad (11)$$

$$\left. \begin{aligned} (lu \times p1) >= p >= (ll \times p1) &\Rightarrow \text{Steady State Condition} \\ \text{else} &\Rightarrow \text{Dynamic Change Condition} \end{aligned} \right\} \quad (12)$$

In dynamic change condition, the change in step size is described as,

$$\left. \begin{aligned} |p-p1| \times 100 &\Rightarrow \left. \begin{aligned} \text{if } \leq 10, &\rightarrow dn = d_{base} / 2 \\ \text{if else } \leq 50 &\rightarrow dn = d_{base} \\ \text{else} &\rightarrow dn = 2 \times d_{base} \end{aligned} \right\} \quad (13) \end{aligned}$$

In steady state condition, store addition of first 3 conjugative duty cycles in variable ' $n$ ' and, after this store addition of second 3 conjugative duty cycles in variable ' $m$ '. Here  $dn$  is calculated as,

$$\left. \begin{aligned} \text{if } |ml - nl| = dn1, &\Rightarrow n = 0, dn = dn1 / 2 \\ \text{else} &, \Rightarrow n = ml, dn = dn1 \end{aligned} \right\} \quad (14)$$

After  $dn$  calculation, follow the logic for optimal duty cycle ( $D$ ) calculation, which is described as,

$$\left. \begin{aligned} \text{if } dv = 0, &\left\{ \begin{aligned} \text{if } di = 0 &\Rightarrow D = D1 \\ \text{elseif } di > 0 &\Rightarrow D = D1 + dn \\ \text{else} &\Rightarrow D = D1 - dn \end{aligned} \right\} \\ \text{else,} &\left\{ \begin{aligned} \text{if } di / dV = -i / V &\Rightarrow D = D1 \\ \text{elseif } di / dV > -i / V &\Rightarrow D = D1 - dn \\ \text{else} &\Rightarrow D = D1 + dn \end{aligned} \right\} \end{aligned} \right\} \quad (15)$$

Where,  $dp = p - p1$ ,  $dV = V - V1$ ,  $di = i - i1$ .  $p$ ,  $V$ ,  $i$ , and  $D$  are the instantaneous PV power, PV voltage, PV current and duty cycle.  $p1$ ,  $V1$ ,  $i1$  and  $D1$  are the just previous (one step delay) PV power, PV voltage, PV current and duty cycle.

The steady-state and dynamic behaviors of the LIC algorithm are shown in Figs.4-5, which shows oscillation reduction in steady state condition and sudden jump, according to the amount of irradiation change in dynamic conditions.

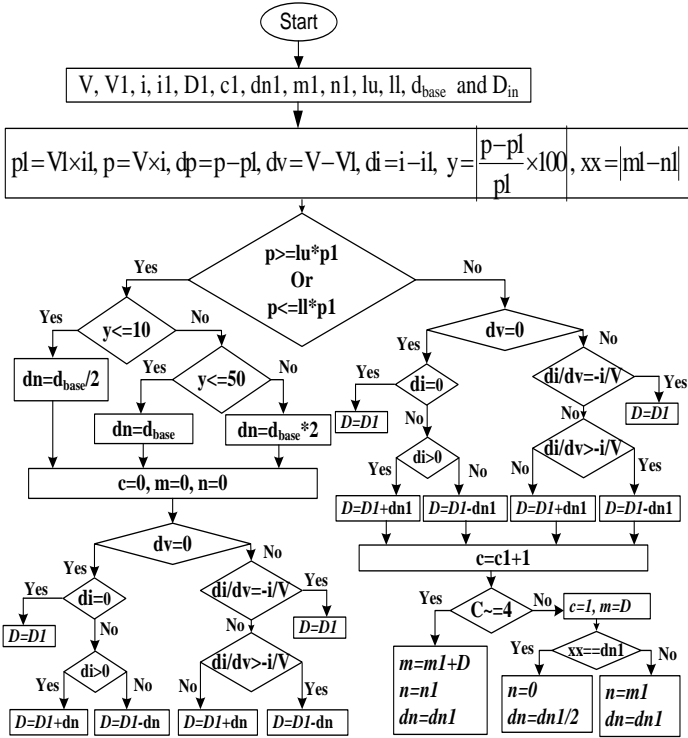


Fig.3 Flowchart of LIC algorithm.

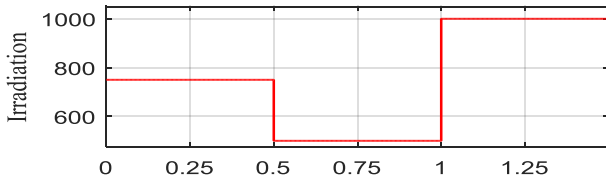


Fig.4 Pattern of solar irradiation variation.

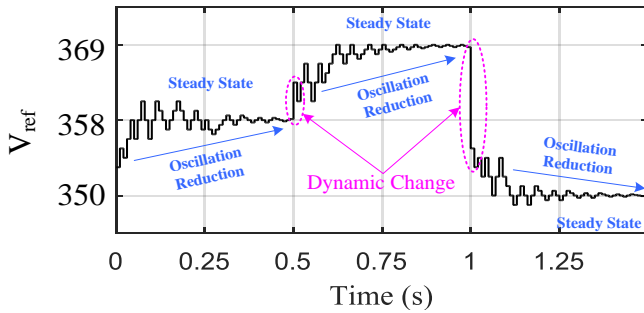


Fig.5 Steady-state and dynamic behavior of LIC algorithm.

### B. Leaky Least Logarithmic Absolute Difference Algorithm

The LLLAD technique is a novel and improved form of LMF (Least Mean Fourth) algorithm, where logarithmic of absolute difference of error is used for quick convergence, and the leaky concept is used for improving the learning process. Schematic of adaptive filter based system identification and weight estimation structure of LLLAD algorithm are shown in Fig.6.

LLLAD smoothly adjusts the conventional cost functions, which minimizes the tracking errors, improves quick pattern recognition, and filter performance. Here, prediction error ( $\phi_a$ ) of active component of load current for phase 'a' is derived as,

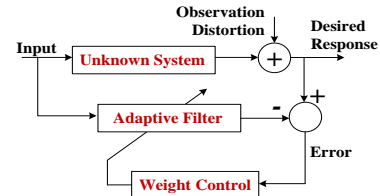


Fig.6 System identification model based on LLLAD.

$$\phi_a(n) = i_{La}(n) - u_a(n) \times \xi_a(n) \quad (16)$$

Through proper adjustment and updating of active weight ( $\xi_a(n)$ ) of load current for phase 'a', the  $\phi_a$  is minimized, which is described as,

$$\xi_a(n+1) = (1 - \Omega \times \mu_a(n)) \times \xi_a(n) + \alpha \times \frac{\mu_a(n) \times u_a(n) \times (\phi_a(n))^3}{1 + \mu_a(n) \times |\phi_a(n)|} \quad (17)$$

Where,  $\Omega$  is leaky learning rate of  $\xi_a(n)$ , and  $\alpha$  is adaptation step size,  $\mu_a(n)$  is designed parameter of phase 'a', which gives an additional degree of freedom. That is calculated as,

$$\mu_a(n+1) = \tau \times \mu_a(n) + \zeta \times \sigma_a(n+1) \quad (18)$$

Where,  $\tau$  and  $\zeta$  are accelerating parameters.  $\vartheta$  is the autocorrelation parameter. For phase 'a', the autocorrelation factor of active component is  $\sigma_a(n)$ , which is described as,

$$\sigma_a(n+1) = \vartheta \times \sigma_a(n) + (1 - \vartheta) \times \phi_a(n) \times \phi_a(n-1) \quad (19)$$

For better understanding and easy implementation, the block diagram of LLLAD, for  $\xi_a(n)$  generation is shown in Fig.7

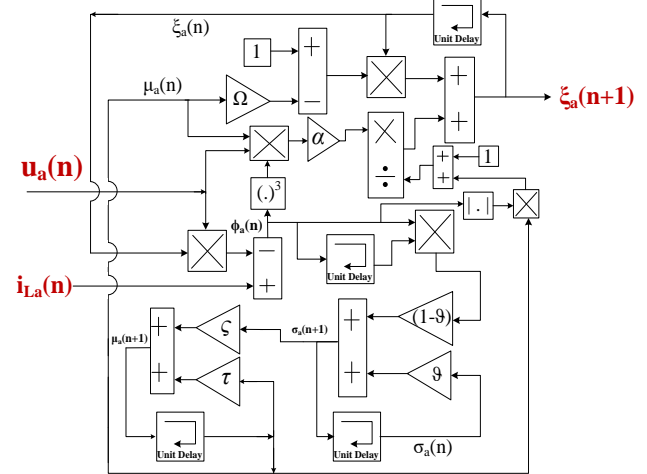


Fig.7 Block diagram of LLLAD algorithm.

In similar way, the active weights ( $\xi_b(n)$ ,  $\xi_c(n)$ ) of load currents for phase 'b' and phase 'c' are generated as,

$$\xi_b(n) = i_{Lb}(n) - u_b(n) \times \xi_b(n) \quad (20)$$

$$\xi_b(n+1) = (1 - \Omega \times \mu_b(n)) \times \xi_b(n) + \alpha \times \frac{\mu_b(n) \times u_b(n) \times (\phi_b(n))^3}{1 + \mu_b(n) \times |\phi_b(n)|}$$

$$\mu_b(n+1) = \tau \times \mu_b(n) + \zeta \times \sigma_b(n+1)$$

$$\sigma_b(n+1) = \vartheta \times \sigma_b(n) + (1 - \vartheta) \times \phi_b(n) \times \phi_b(n-1)$$

$$\xi_c(n) = i_{Lc}(n) - u_c(n) \times \xi_c(n) \quad (21)$$

$$\xi_c(n+1) = (1 - \Omega \times \mu_c(n)) \times \xi_c(n) + \alpha \times \frac{\mu_c(n) \times u_c(n) \times (\phi_c(n))^3}{1 + \mu_c(n) \times |\phi_c(n)|}$$

$$\mu_c(n+1) = \tau \times \mu_c(n) + \zeta \times \sigma_c(n+1)$$

$$\sigma_c(n+1) = \vartheta \times \sigma_c(n) + (1 - \vartheta) \times \phi_c(n) \times \phi_c(n-1)$$

The control structure for  $\xi_a(n)$ ,  $\xi_b(n)$ ,  $\xi_c(n)$  is shown in Fig.8.



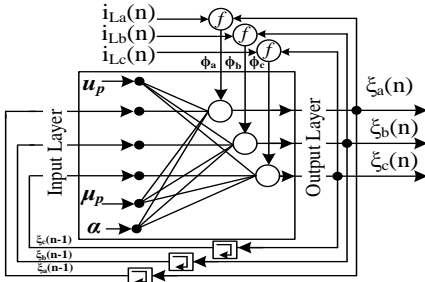


Fig.8 The control structure of weight updating process.

### C. Comparative Analysis of Proposed LLLAD Algorithm

The comparative analysis of proposed LLLAD control algorithm with most popular adaptive algorithms, such as LMS (Least Mean Square), LMF (Least Mean Fourth), LLMF (Leaky Least Mean Fourth) and normalized LMS (NLMS) is shown in Fig.9.

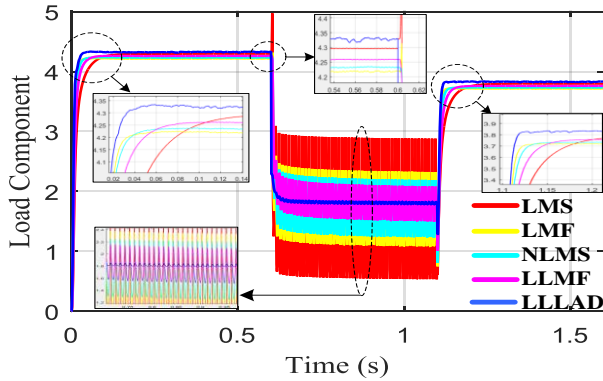


Fig.9 Responses of different algorithms.

For comparative analysis, the unbalanced load situation, where the outage of one phase of load for a period of 0.6s to 1.1s, is considered. Fig.9 shows a comparison in responses of fundamental load component extraction from the load current, which is the resultant active weight component ( $\Phi_p$ ). In term of oscillations, Fig.9 shows that during load unbalance, the highest oscillations are in LMS and lowest in LLLAD. Similarly, in terms of settling time and accuracy, Fig.9 depicts that higher settling time and lower accuracy are in LMF, while lower settling time and higher accuracy are in LLLAD, which shows a very good fundamental load component extraction ability of LLLAD algorithm.

## IV. RESULTS AND DISCUSSION

A prototype of the system is developed for performance evaluation of LLLAD based control technique, as shown in Fig.10. To realize the PV characteristic, a solar PV simulator (AMETEK, ETS600x17DPVF) is used, and it is integrated to the actual grid. During integration, for PV power conversion in AC form, load feeding, and for synchronization, a three-phase voltage source converter (VSC) is used. Moreover, for MPPT operation, a novel LIC MPPT algorithm is used, which operates the boost converter. The RC filter and interfacing inductors are used for harmonics and switching ripples mitigation. A DSpace (Digital Signal Processor for Applied and Control Engineering) controller (1202-DSPACE) is used for execution of control techniques. Hall-Effect current (LA-55p) and voltage (LV-25) sensors are used for sensing all signals. For voltage and current measurement, a multimeter (Fluke-115) is used. A set of power quality analyzers (Fluke-

43B and Hioki-3100) is used for analysis of different harmonic spectra. Differential voltage probes (HAMEG-115Hz) and current probes (Tektronix-A622) are used for voltage and current measurement. A digital storage oscilloscope (DSO7014A) is used for dynamic performance analysis. The converter parameters are given in Table I.

The system parameters are,  $V_{oc}=220V$ ,  $I_{sc}=16A$ ,  $P_{load}=860W$ ,  $v_g=150V$ ,  $f=50Hz$ ,  $L_{in}=5mH$ ,  $C_{fl}=10\mu F$ ,  $R_{fl}=10\Omega$ ,  $\vartheta=0.2$ ,  $\tau=0.001$ ,  $\zeta=0.00001$ ,  $\Omega=0.002$ ,  $r_{base}=2V$ ,  $d_{base}=0.01$ ,  $\alpha=1$ ,  $\theta=1.1$ .

TABLE I. CONVERTER PARAMETERS

Boost Converter		Voltage Source Converter	
Parameter	Selected Value	Parameter	Selected Value
Inductor	3.5mH	AC Voltage Rating	415V
Commutation Frequency	20 kHz	DC Voltage Rating	750V
DC Bus Capacitor	1000 $\mu F$	Capacitor	2100 $\mu F \times 2$
Mode of Operation	Continuous	Switching Frequency	40 kHz

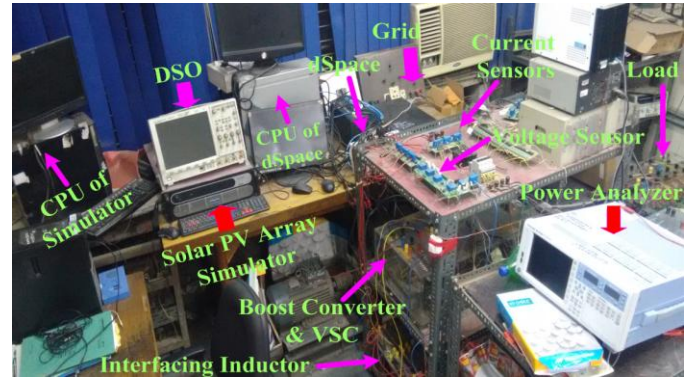


Fig.10 Photograph of the developed prototype.

### A. Operation under Normal Condition

The steady-state responses of phase 'a' are shown in Fig.11, where loads are nonlinear.

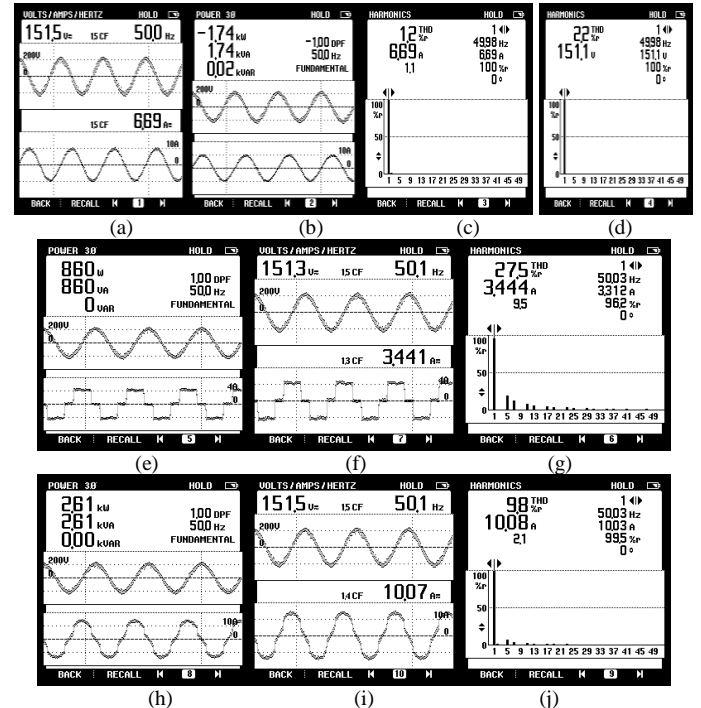


Fig.11 Waveform of steady-state response for phase 'a', (a)-(d) voltage, current and THD of grid current and voltage, (e)-(g) voltage, current and THD of load current, and (h)-(j) voltage, current and THD of VSC current.

Figs.11(e)-(g) show that successfully power demand of the nonlinear load (Rectifier followed R-L load) is satisfied, which current THD is 27.5%. Moreover, Figs.11(a)-(d) show that after fulfill the load demand, extra 1.74kW power is fed to the grid, where THD of the grid voltage and current are 2.2% and 1.2%, which is well within the permissible limit of 5% according to the IEEE-519 standard [22]. Figs.11(h)-(j) show the waveforms of VSC power, which is supplied by solar PV array and consumed by the load as well as fed to the grid. The THD of VSC current is 9.8%. It shows that VSC supplies required harmonics at PCC to the nonlinear load. Therefore, grid currents are found sinusoidal having THD within the limit.

### B. Operation under Load Unbalanced Condition

During unbalanced load condition, the load of phase 'a' is removed, and its dynamic impact on phase 'a' and phase 'b', is shown in Fig.12(a), and Fig.12(b), respectively, as well as internal signals, are shown in Fig.12(c).

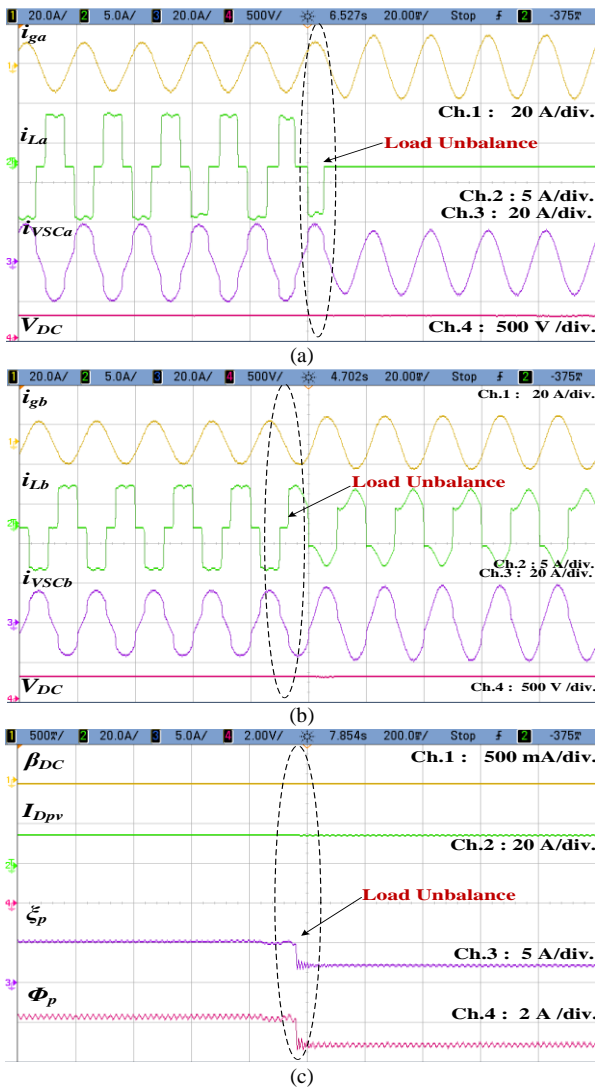


Fig.12 Waveforms during load unbalance, (a)-(b) grid current, load current, VSC current and DC link voltage of phase 'a' and 'b', (c) internal signals.

Fig.12(a) shows that the load of phase 'a' is removed, so the load current becomes zero. However, due to proper control action, grid currents are balanced and sinusoidal, and DC link voltage is constant. Since, due to outage of phase 'a' load, the requirement of harmonics current is reduced, so the shape of

VSC current is improved and becomes sinusoidal, as well as nonlinearity of the phase 'b' load current is also reduced, which is shown in Fig.12(b). The performance of internal signals during dynamic condition is shown in Fig.12(c), which shows that the DC loss component ( $\beta_{DC}$ ) is very low, due to balanced DC link voltage. Moreover, PV array power dynamic reflection component ( $I_{Dpv}$ ) is constant, because solar irradiation is assumed constant, and estimated active weight component ( $\xi_p$ ) is reduced as the requirement of active power is reduced. Therefore, the resultant of all components ( $\Phi_p$ ), is also reduced.

### C. Operation during Solar PV Array Irradiation Variation

During solar insolation variation condition, it is tested for insolation fall (from  $1000\text{W/m}^2$  to  $800\text{W/m}^2$ ), as well as tested for insolation rise (from  $800\text{W/m}^2$  to  $1000\text{W/m}^2$ ). The steady-state performances, at solar irradiance  $1000\text{W/m}^2$  and  $800\text{W/m}^2$  are shown in Fig.13. The dynamic performances for irradiation fall and irradiation rise are given in Fig.14.

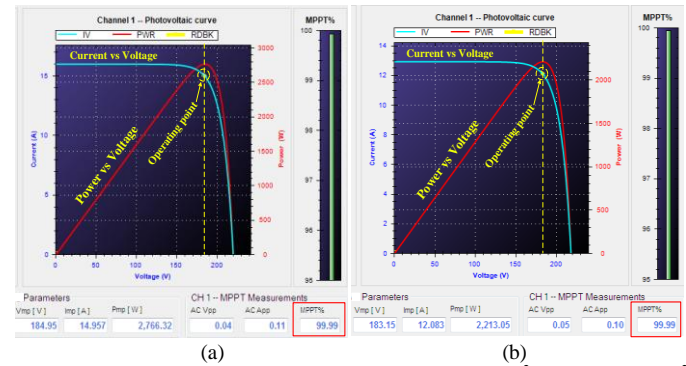


Fig.13 Steady-state performance at insolation (a)  $1000\text{W/m}^2$ , and (b)  $800\text{W/m}^2$ .

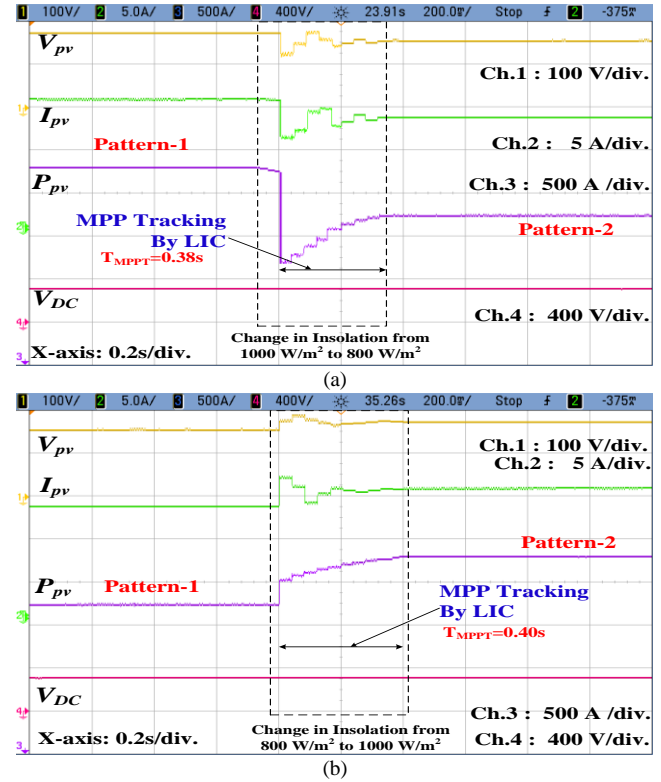


Fig.14 Waveforms of LIC, during (a) insolation fall and (b) insolation rise.

Fig.14 shows a very smooth and quick maximum power point tracking performance, which is possible only due to proposed LIC algorithm. Moreover, the steady-state

performances in insolation rise and fall condition, at irradiation 1000W/m<sup>2</sup> and 800W/m<sup>2</sup> are oscillation free, which is only due to learning based duty cycle reduction process of LIC algorithm. After irradiation change, it has taken approximately 0.39s to track the MPP, which shows the excellent dynamic performance of proposed MPPT technique. In both conditions, the tracking efficiencies are 99.99% and 99.99%, which are shown in Fig.13 as well as the red boundary on Fig.13 highlights the %MPPT. These MPPT efficiencies are approximately close to 100%, which shows the accuracy of the LIC algorithm.

### 1) Comparative MPPT Analysis with State of Art Technique

On same circuitry condition, for comparative analysis, the most recent technique is considered, which is modified power ratio variable-step based P&O algorithm (MPRVPO) [23]. The obtained waveforms of MPRVPO algorithm for irradiation fall and irradiation rise condition are shown in Fig.15.

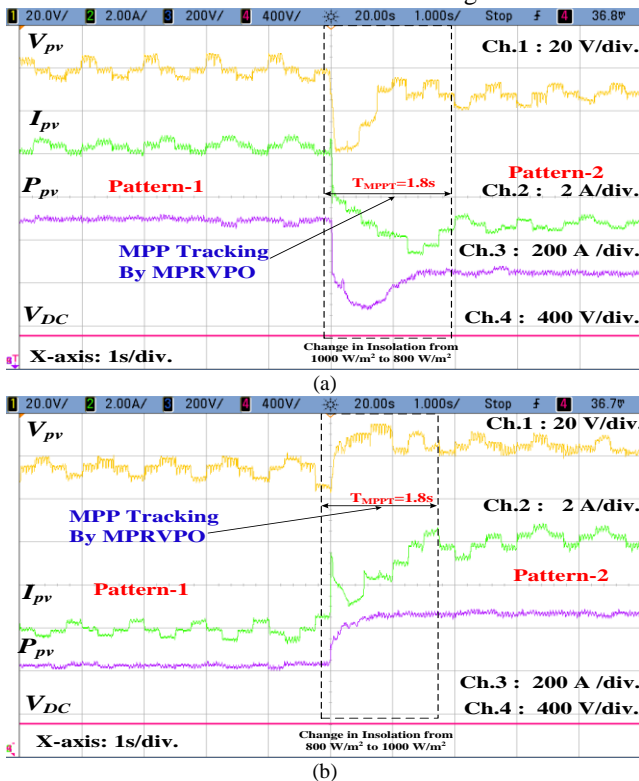


Fig.15 Waveforms of MPRVPO algorithm during (a) insolation fall and (b) insolation rise condition.

Fig.14 and Fig.15 show that LIC algorithm and MPRVPO algorithm, both MPPT algorithms are capable to track the MPP. However, the average tracking duration of MPRVPO algorithm is 1.8s, while LIC algorithm has reached the GMM only in 0.39s. Moreover, waveforms clearly show that the steady state oscillation in MPRVPO algorithm is very high, while in LIC algorithm, it is negligible. Therefore, LIC MPPT algorithms shows the superiority on state of the art techniques.

### D. Operation under Grid-Voltage Fluctuations Condition

During testing for grid voltages fluctuation, the overvoltage condition is considered. In this condition, the fluctuation in grid voltage of approximately 10% is taken, which test responses of phase 'a' are shown in Fig.16. Moreover, harmonics spectra of grid current of the phase 'a' are shown in Fig.17.

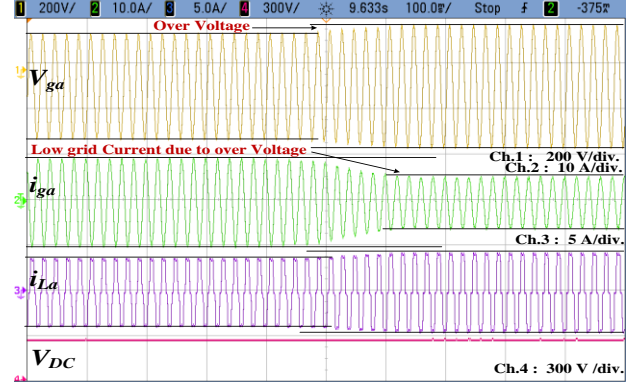


Fig.16 Waveforms during over-voltage condition.

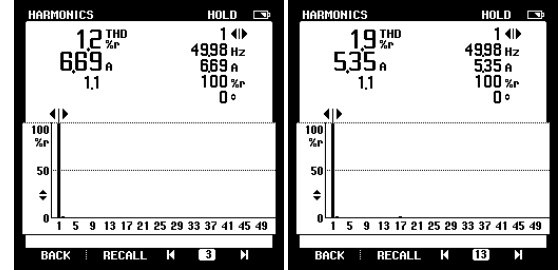


Fig.17 Harmonics spectra of grid current for phase 'a', during (a) normal condition, and (b) overvoltage condition.

The waveforms of overvoltage depict that, the voltage at PCC is increased, so due to constant supply power, the  $i_{ga}$  is decreased. Moreover, since  $P_L$  (load power) is directly proportional to the square of  $v_{PCC}$  (PCC voltage), so  $P_L$ , as well as  $i_L$ , is increased. However, due to strong control ability, the  $V_{DC}$  is regulated to the desired value, and a balanced power is fed to the load, which is shown in Fig.16. Moreover, after fulfill the load demand, the extra power is supplied to the grid. During this process, the THD of  $i_{ga}$  is still low and within the permissible limit of 5% according to the IEEE-519 standard[22][24], which is shown in Fig.17. Similarly, during under-voltage condition, the power management and the THD of grid currents are good and within the permissible limit.

### E. Operation during Grid Voltage Imbalance Condition

The dynamic behavior of the system under the imbalance grid voltages condition, is shown in Fig.18 and vector diagram of all components are shown in Fig.19.

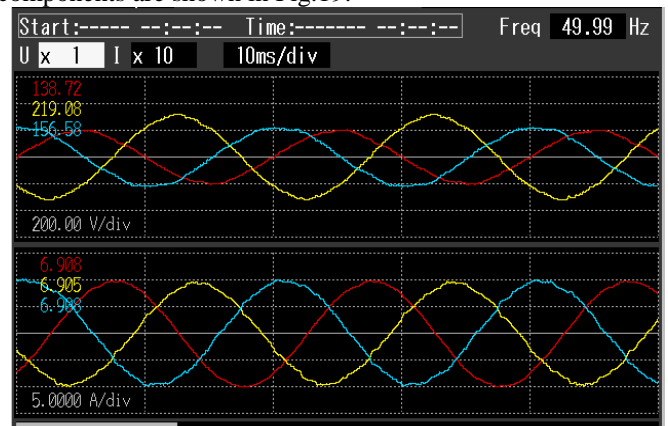


Fig.18 Waveforms of three-phase voltage and current during phase imbalance. From Figs.18-19, it is visible that three phase voltages are 138.13V, 218.73V and 155.84V, which is a highly imbalance



condition. Moreover, Fig.19 shows that a phase angle difference, between grid voltages, is not  $120^\circ$ , which depicts the phase angle imbalance. However, in this situation, three phase currents are 6.906A, 6.900A, and 6.903A, and the phase angle difference, between the grid currents, is  $120^\circ$ , which show balanced supply currents. Moreover, the THDs of grid currents are below 5%, which shows a satisfactory performance.

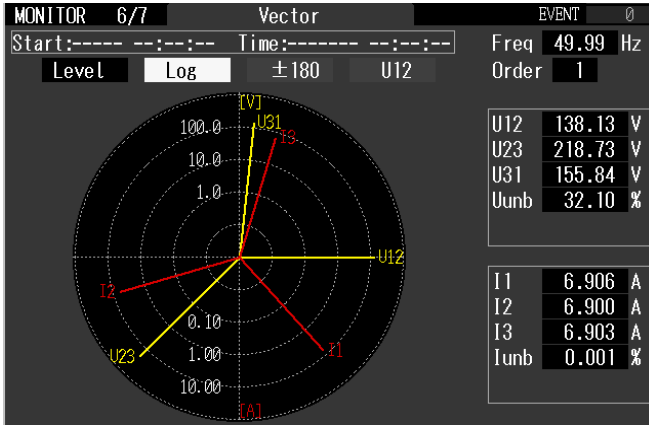


Fig.19 Vectors of three-phase voltage and current during phase imbalance.

#### F. Operation during Grid Voltage Distortion Condition

Performances under grid voltage distortion condition for phase 'a', are shown in Fig.20, and analyzed by using a power analyzer, which obtained waveforms are shown in Fig.21.

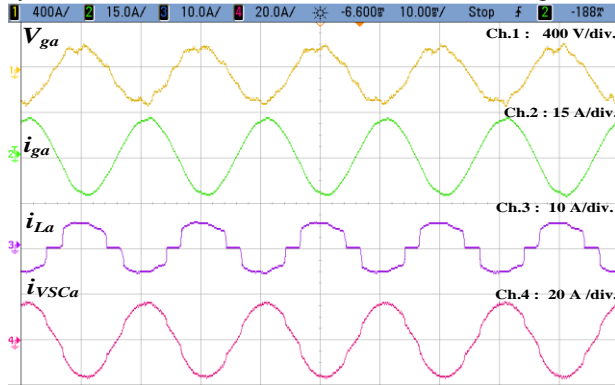
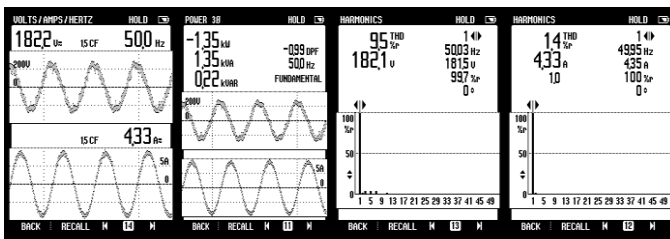
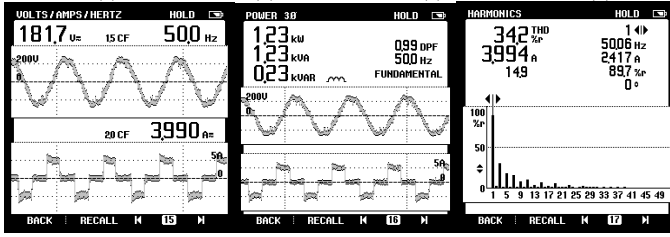


Fig.20 Waveforms under grid voltage distortion condition.



(a) (b) (c) (d)



(e) (f) (g)

Fig.21 Waveforms of, (a)-(d) phase 'a' grid voltage, current, power and its harmonics spectrum, and (e)-(f) phase 'a' load voltage, current, power and its harmonics spectrum, during grid voltage distortion condition.

Here THDs of distorted  $v_{ga}$  and THD of nonlinear load current are 9.5%, and 34.2%, which are shown in Fig.21(c) and Fig.21(g), respectively. Moreover, for testing of proposed control technique in a highly complex situation, the overvoltage condition is applied, at distorted grid voltage condition. In this highly nonlinear situation, the proposed control technique has performed very well and properly fed the load. After fulfill the load demand, an extra power is transferred to the grid, where THD of grid current is only 1.4%, with unity power factor, as is shown in Fig.21(d).

#### 1) Comparative Analysis under Distorted Grid Voltage and Nonlinear Load Condition with State of Art Techniques

For comparative analysis, on the same circuitry condition, the most popular techniques, ANF, KF and proposed LLLAD technique are tested. During testing, the nonlinear load is connected, at PCC and distorted grid voltage situation is taken. Here the objective of the controller is, first the load is fed, and after feeding the load, the rest power is supplied to the grid. In this situation, the achieved THD of  $i_{ga}$  by using ANF based control technique is very poor, that is 4.7%. Moreover, in the case of KF based control technique, the THD of  $i_{ga}$  is improved, that is 3.8%. However, the obtained THD of  $i_{ga}$  by using LLLAD technique is only 1.4%, which depicts a significant difference, in comparison to state of art techniques.

#### G. Operation during Day-to-Night Mode

In day-to-night condition, during the daytime, solar PV power is used to meet the load demand, and if some power is left, then it is fed into the grid. Moreover, during the night time, when solar power is zero, then the load demand is met by taking power from the grid, and VSC acts as a DSTATCOM, which provides reactive power support. These all performances for day-to-night mode, are shown in Figs.22-23 and for night-to-day mode are shown in Figs.24-25.

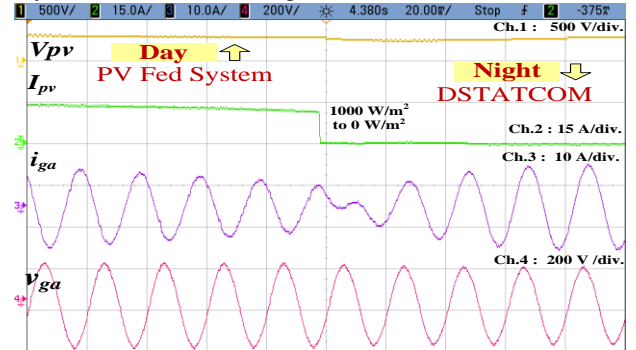


Fig.22 Waveforms of PV and grid, during day-to-night mode of operation.

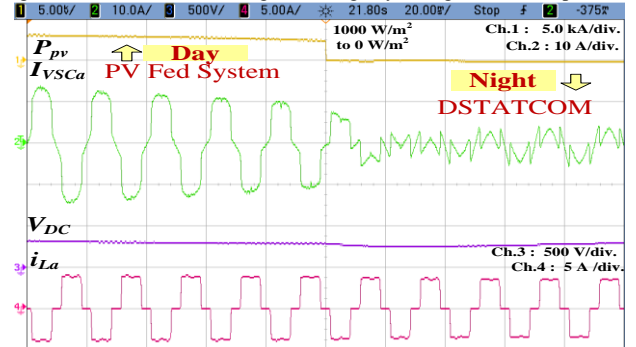


Fig.23 Waveforms of PV and VSC, during the day-to-night mode of operation.



In Fig.22 and Fig.24, during the daytime,  $i_{ga}$  and  $v_{ga}$  are out of phase, which shows that the power is fed into the grid. Moreover, during night time,  $i_{ga}$  and  $v_{ga}$  are in the same phase, which shows that power is supplied from the grid.

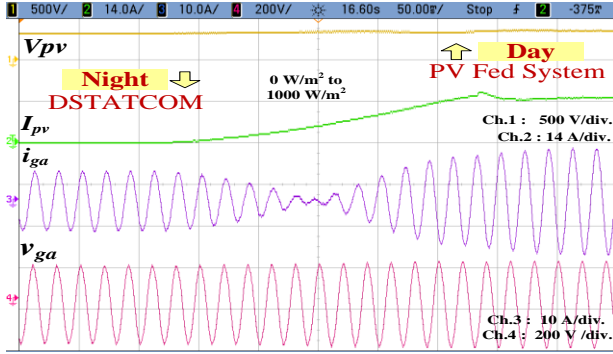


Fig.24 Waveforms of PV and grid, during night-to-day mode of operation.

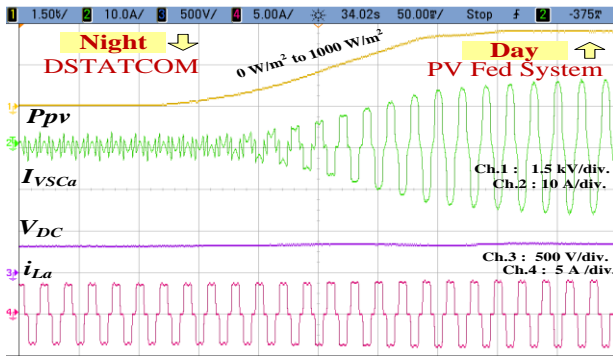


Fig.25 Waveforms of PV and VSC, during the night-to-day mode of operation.

The compensation behavior of VSC at night time is shown in Fig.23 and Fig.25, where it behaves like DSTATCOM. It increases the utility of the system. Moreover, in both conditions, the DC link voltage is maintained, which has only possible due to the strong controlling ability of the LLLAD based VSC control and LIC based MPPT algorithm.

## V. CONCLUSION

A novel control technique namely Leaky Least Logarithmic Absolute Difference (LLLAD) based control algorithm and Learning based Incremental Conductance (LIC) MPPT (Maximum Power Point Tracking) algorithm, for grid-tied solar PV system have been developed and implemented on the developed prototype, where the nonlinear/linear loads have been connected at PCC. The MPPT by LIC has been shown the very good steady-state as well as dynamic performance on different irradiation conditions. The LLLAD control enhances the power management ability with improved power quality, for a two-stage three-phase grid integrated solar PV system, where distribution network is subjected to nonlinear loading at, under-voltage, over-voltage, phase imbalance and the distorted voltage at PCC. The simple architecture of the LLLAD makes easy to implement and helps in computational complexity reduction as well as quick dynamic performance. The performance of LLLAD has also been evaluated on day to night mode of operation. During daytime, the system behaves as PV tied grid system, where control technique provides load balancing, power factor correction, harmonics filtering and mitigation of other power quality issues. However, when solar irradiation is zero, in the night time, DC link capacitor and VSC act as DSTATCOM, which enhances the utilization factor

of the system. Test results have shown its satisfactory performance at unity power factor (UPF) under abnormal grid conditions, such as distortion in grid voltage at nonlinear and unbalanced load at PCC. Moreover, THDs in grid voltages and grid currents have been observed within permissible limit, according to the IEEE-519 standard.

## REFERENCES

- [1] G. Velasco-Quesada, F. Guinjoan-Gispert, R. Pique-Lopez, M. Roman-Lumbreras and A. Conesa-Roca, "Electrical PV Array Reconfiguration Strategy for Energy Extraction Improvement in Grid-Connected PV Systems," *IEEE Trans. Industrial Electronics*, vol. 56, no. 11, pp. 4319-4331, Nov. 2009.
- [2] A. Sangwongwanich, Y. Yang and F. Blaabjerg, "A Sensorless Power Reserve Control Strategy for Two-Stage Grid-Connected PV Systems," *IEEE Trans. Power Electr.*, vol. 32, no. 11, pp. 8559-8569, Nov. 2017.
- [3] E. Roman, R. Alonso, P. Ibanez, S. Elorduizapatarietxe and D. Goitia, "Intelligent PV Module for Grid-Connected PV Systems," *IEEE Trans. Industrial Electronics*, vol. 53, no. 4, pp. 1066-1073, June 2006.
- [4] S. Somkun and V. Chungak, "Unified Unbalanced Synchronous Reference Frame Current Control for Single-Phase Grid-Connected Voltage-Source Converters," *IEEE Trans. Industrial Electronics*, vol. 63, no. 9, pp. 5425-5436, Sept. 2016.
- [5] P. García, C. A. García, L. M. Fernández, F. Llorens and F. Jurado, "ANFIS-Based Control of a Grid-Connected Hybrid System Integrating Renewable Energies, Hydrogen and Batteries," *IEEE Trans. Industrial Informatics*, vol. 10, no. 2, pp. 1107-1117, May 2014.
- [6] X. Fu and S. Li, "Control of Single-Phase Grid-Connected Converters With LCL Filters Using Recurrent Neural Network and Conventional Control Methods," *IEEE Trans. Power Electronics*, vol. 31, no. 7, pp. 5354-5364, July 2016.
- [7] T. Z. Bei and P. Wang, "Robust frequency-locked loop algorithm for grid synchronisation of single-phase applications under distorted grid conditions," *IET Gen., Trans. & Dist.*, vol. 10, no. 11, pp. 2593-2600, April 2016.
- [8] H. Yi, X. Wang, F. Blaabjerg and F. Zhuo, "Impedance Analysis of SOGI-FLL-Based Grid Synchronization," *IEEE Trans. Power Electronics*, vol. 32, no. 10, pp. 7409-7413, Oct. 2017.
- [9] R. Panigrahi and B. Subudhi, "Performance Enhancement of Shunt Active Power Filter Using a Kalman Filter-Based  $H_\infty$  Control Strategy," *IEEE Trans. Power Electr.*, vol. 32, no. 4, pp. 2622-2630, April 2017.
- [10] C. A. Busada, S. Gomez Jorge, A. E. Leon and J. A. Solsona, "Current Controller Based on Reduced Order Generalized Integrators for Distributed Generation Systems," *IEEE Trans. Industrial Electronics*, vol. 59, no. 7, pp. 2898-2909, July 2012.
- [11] H. Karimipour and V. Dinavahi, "Extended Kalman Filter-Based Parallel Dynamic State Estimation," *IEEE Trans. Smart Grid*, vol. 6, no. 3, pp. 1539-1549, May 2015.
- [12] G. Rigatos, P. Siano, N. Zervos and C. Cecati, "Decentralised control of parallel inverters connected to microgrid using the derivative-free nonlinear Kalman filter," *IET Power Electr.*, vol. 8, no. 7, pp. 1164-1180, July 2015.
- [13] C. A. Rojas, M. Aguirre, S. Kouro, T. Geyer and E. Gutierrez, "Leakage Current Mitigation in Photovoltaic String Inverter Using Predictive Control With Fixed Average Switching Frequency," *IEEE Trans. Industrial Electronics*, vol. 64, no. 12, pp. 9344-9354, Dec. 2017.
- [14] A. Vidal, F. D. Frejedo, A. G. Yepes, J. Malvar, Ó. López and J. Doval-Gandoy, "Transient response evaluation of stationary-frame resonant current controllers for grid-connected applications," *IET Power Electronics*, vol. 7, no. 7, pp. 1714-1724, July 2014.
- [15] M. A. Elgendy, B. Zahawi and D. J. Atkinson, "Assessment of the Incremental Conductance Maximum Power Point Tracking Algorithm," *IEEE Trans. Sustainable Energy*, vol. 4, no. 1, pp. 108-117, Jan. 2013.
- [16] J. Ahmed and Z. Salam, "A Modified P&O Maximum Power Point Tracking Method With Reduced Steady-State Oscillation and Improved Tracking Efficiency," *IEEE Trans. Sust. Ener.*, vol. 7, no. 4, pp. 1506-1515, Oct. 2016.
- [17] A. Thangavelu, S. Vairakannu and D. Parvathyshankar, "Linear open circuit voltage-variable step-size-incremental conductance strategy-based hybrid MPPT controller for remote power applications," *IET Power Electronics*, vol. 10, no. 11, pp. 1363-1376, Sep. 2017.
- [18] M. Rakhshan, N. Vafamand, M. Khooban and F. Blaabjerg, "Maximum Power Point Tracking Control of Photovoltaic Systems: A Polynomial

- Fuzzy Model-Based Approach," *IEEE Journal of Emerging and Selected Topics in Power Electronics*, vol. 6, no. 1, pp. 292-299, March 2018.
- [19] K. Jyotheeswara Reddy and N. Sudhakar, "High Voltage Gain Interleaved Boost Converter With Neural Network Based MPPT Controller for Fuel Cell Based Electric Vehicle Applications," *IEEE Access*, vol. 6, pp. 3899-3908, June 2018.
- [20] C. Jain and B. Singh, "An Adjustable DC Link Voltage Based Control of Multifunctional Grid Interfaced Solar PV System," *IEEE Journal of Emer. and Sel. Topics in Power Electron.*, vol. 10, no. 3, pp. 112-121, May 2016.
- [21] N. Kumar, I. Hussain, B. Singh and B. K. Panigrahi, "Normal Harmonic Search Algorithm Based MPPT for Solar PV System and Integrated with Grid using Reduced Sensor Approach and PNKLMS Algorithm," *IEEE Trans. Industry Appl.*, vol. 54, no. 6, pp. 6343-6352, Nov.-Dec. 2018.
- [22] IEEE Draft Guide for Applying Harmonic Limits on Power Systems," *IEEE P519.1/D12, July 2012*, pp.1-124, Feb. 2015.
- [23] M. Rezkallah, A. Chandra, M. Tremblay and H. Ibrahim, "Experimental Implementation of an APC with Enhanced MPPT for Standalone Solar Photovoltaic based Water Pumping Station," *IEEE Trans. Sustainable Energy*, 2018 (Early Access).
- [24] N. Kumar, B. Singh and B. Panigrahi, "Grid Synchronization Framework for Partially Shaded Solar PV Based Microgrid using Intelligent Control Strategy," *IET Generation, Transmission & Distribution*, 2018. (IEEE Early Access Articles, Oct. 2018).